Nanoscale

Accepted Manuscript

This article can be cited before page numbers have been issued, to do this please use: R. Hao, L. Zhang, L. Zhang, H. You, J. Fan and J. Fang, *Nanoscale*, 2020, DOI: 10.1039/D0NR01130D.

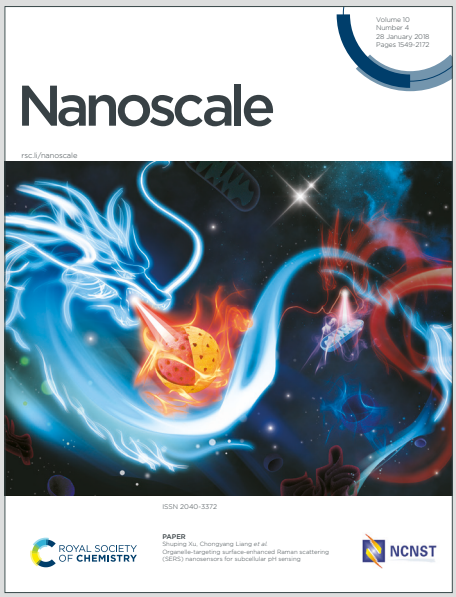

ROYAL SOCIETY OF CHEMISTRY

rsc.li/nanoscale

View Article Online
DOI: 10.1039/D0NR01130D

Curved 2D WS_2 Nanostructures: Nanocasting and Silent Phonon Mode

Rui Hao,[a] Lingling Zhang,[a] Lei Zhang,*[a] Hongjun You,[b] Jie Fan[c] and Jixiang Fang*[a]

[a]Key Laboratory of Physical Electronics and Devices of Ministry of Education, School of Electronic Science and Engineering, Xi'an Jiaotong University, Xi'an 710049, China.

E-mail: jxfang@mail.xjtu.edu.cn; eiezhanglei@xjtu.edu.cn

[b]School of Science, Xi'an Jiaotong University, Xi'an 710049, China

[c]Prof. J. Fan, Key Lab of Applied Chemistry of Zhejiang Province, Department of Chemistry, Zhejiang University, Hangzhou 310027, China

View Article Online
DOI: 10.1039/D0NR01130D

Abatract: Layered two-dimensional (2D) materials and their heterostructures possess excellent optoelectronic properties due to their unique planar features. However, planar structures can only selectively support the fundamental optical modes, which is averse to fully exploit the potentials of the 2D materials. Here, a novel type of tungsten disulfide (WS_2) nanoparticles (NPs) with uniform size and morphology and highly ordered WS_2 supercrystals (SCs) are synthesized by nanocasting process using ordered mesoporous silica as template. Due to the curved feature of individual nanostructures, their Raman signals show complex dependence behavior on the excitation wavelength, excitation power and temperature. Significantly, the silent phonon mode becomes Raman active due to the curvature of the interlaced WS_2 layers. We believe that curved features will greatly enrich the optoelectronic applications of 2D materials.

View Article Online
DOI: 10.1039/D0NR01130D

1. Introduction

Two-dimensional (2D) materials, such as graphene, transition-metal dichalcogenides (TMDCs), boron-nitride (BN) and their layered heterostructures, have attracted great attention in recent years owing to their intriguing properties related to the unique lower dimensional features.[1-3] In particular, TMDCs show great potential in electronic and optical devices due to their direct band gaps.[4,5] In addition to sizes, shapes, thickness and crystal qualities of 2D materials,[6,7] different geometric dimension features can also greatly influence their properties. For example, by directly growing graphene on complex three-dimensional (3D) pillars, high-order plasmonic modes could be excited due to the strong field localization at the sidewall graphene,[8] which can greatly enhance infrared (IR) signals for sensing applications.[9] It is thus believed that layered materials with curved features have promising potentials to extend the applications of 2D materials in comparison with normal lamellar counterparts. Thereinto, nanoparticles (NPs) and their array structures consisting of layered materials are a class of special structures due to the curved layers in spherical structure, which may lead to excellent properties.[10,11]

Basically, the primitive unit cell of TMDCs of the form MX_2 consist of two metal (M) atoms and four chalcogen (X) atoms. M and X atoms are strongly linked via covalent bonds to form a monolayer structure, while several monolayers can be stacked loosely via var der Waals interaction to form a multilayer structure. Different vibration motions of atoms result in various optical and acoustic phonon modes, which could be characterized by Raman spectroscopy and employed to investigate the inherent molecule structures.[12-13] Previously, the phonon properties of atomically thin MX_2 have been investigated via Raman spectroscopy by varying the external environment, such as the heating effect, strain and the excitation conditions.[14-16] Significantly, the thicknesses of MX_2 can be identified by analyzing the change in different Raman peaks.[17,18] However, most of the related studies concentrate on 2D layered MX_2 structures.[19,20] In contrast, the vibration motion of

View Article Online
DOI: 10.1039/D0NR01130D

MX_2 atoms may be deformed, which could thus introduce novel Raman features due to the introduction curvatures and deformations.

Since the discovery of tungsten disulfide (WS_2) and molybdenum disulfide (MoS_2) NPs,[21,22] a variety of methods including arc discharge,[23] chlorides,[24] laser ablation,[25] microwave plasma,[26] chemical vapor transport[27] and spray pyrolysis[28] are utilized to synthesize 2D materials with spherical structures. However, these processes are usually both time and energy consuming, and the sizes and morphologies of these structures are hardly to be accurately controlled, which limit their practical applications. Here, we exploit a strategy to synthesize two types of WS_2 with curved morphology, *i.e.*, WS_2 NPs and highly ordered supercrystals (SCs), using ordered mesoporous silica, EP-FDU-12, as a template by means of nanocasting method. The uniform pores in the EP-FDU-12 template can limit the growth of WS_2 layers in the spherical cell to form the uniform WS_2 NPs and WS_2 SCs. The Raman signals of the obtained WS_2 NPs and WS_2 SCs are investigated by varying the laser power, laser wavelength and experimental temperature. Interestingly, we find the silent B_{1u} mode becomes activated in WS_2 NPs and WS_2 SCs.

2. Results and Discussion

Structural characterization

In order to synthesize WS_2 nanostructures with uniform morphology and size, an ordered mesoporous silica, EP-FDU-12, is selected as the hard template, which possesses a uniform cage type pore system with large spherical cells. The average diameter of the pores is about 27 nm (Figure S1). These structural features of EP-FDU-12 silica template display several vital advantages for nanocasting process. The uniform mesopores are ideal templates for synthesis of inverse structures and the WS_2 layers can be completely confined in the uniform spherical cells to form WS_2 NP and SC structures. Furthermore, the individual NPs with a large spherical size are preferably obtained via high-temperature reductive sulfuration process using EP-FDU-12 as the

View Article Online
DOI: 10.1039/D0NR01130D

hard template.[29-31] During the nanocasting processes, the phosphotungstic acid (PTA) precursor is incorporated into the EP-FDU-12 silica template via a solvent evaporation process firstly. Then the PTA/silica composites are *in situ* sulfurated by H_2S gas. After the removal of silica template, WS_2 NPs and SCs with different structures can be fabricated by controlling the filling amount of PTA (Figure 1).

A typical morphology of WS_2 NPs is shown in Figure 2. The scanning electron microscopy (SEM) image (Figure 2a) shows that WS_2 NPs display a monodispersed spherical structure with good uniformity. The average diameter of WS_2 NPs is about 26 nm, which is close to the size of the spherical cells of EP-FDU-12 silica template. From the transmission electron microscopy (TEM) images (Figures 2b and 2c), it is found that these WS_2 NPs are constituted by disordered and curved multilayered WS_2. The high-resolution TEM (HRTEM) image indicates that the interlayer distance is around 0.67 nm. The selected-area electron diffraction (SAED) pattern (Figure 2d) confirms the polycrystalline structure of WS_2 NPs. The diffraction peaks in the X-ray diffraction (XRD) pattern (Figure 2e) are indexed by (002), (004), (101), (103), (105), (008), and (201) corresponding to standard WS_2 crystal (JCPDS card No: 08-0237). No other diffraction peaks belonging to PTA, W, WO_3 or WO_2 are observed, indicating a complete transformation from PTA to WS_2.

The morphology of WS_2 NPs can be tailored by controlling the filling amount of PTA. Three types of WS_2 NPs, *i.e.*, bowl-like, half-spherical and spherical structures, are shows in Figure 3, which correspond to the PTA concentrations of 5, 10 and 20 mM, respectively. The synthesized WS_2 NPs under various filling amount of PTA have a good uniformity of diameter with a value of around ~26 nm. As shown in Figures 3a and 3b, the bowl-like WS_2 NPs consist of 8-12 curved layers arranged along the spherical cell wall. For half-spherical WS_2 NPs structures, some WS_2 layers fill in the WS_2 bowls randomly (Figures 3d and 3e). In contrast, the WS_2 spherical NPs

View Article Online
DOI: 10.1039/D0NR01130D

consist of disordered and crooked WS_2 sheets in the whole spherical cells (Figures 3g and 3h). The schematics of the synthesized WS_2 NPs are shown in Figures 3c, 3f and 3i, respectively.

Figure 4 shows the morphology and structure of WS_2 SCs synthesized with 30 mM filling concentrations of PTA. From the SEM image (Figure 4a), it is found that the average size of WS_2 SCs is around 5-10 μm. The individual WS_2 SC and the enlarged images show a well-organized close-packed array consisting of tetragonal and hexagonal arranged WS_2 NPs (Figures 4b and 4c). The HRTEM images demonstrate the structural features of typical array with the uniform WS_2 NP size of 28 nm in diameter (Figures 4d and 4e). The ordered WS_2 NP arrays are constituted by disordered and curved multilayered WS_2 layers with an interlayer distance of around 0.67 nm (Figure 4d). The SAED pattern shows the polycrystalline feature of WS_2 SCs (Figure 4f). XRD pattern of WS_2 SCs clearly shows that all the diffraction peaks agree well with the standard WS_2 structure (JCPDS Card No. 08-0237) and can be assigned to the (002), (004), (101), (103), (105), (110), (112), (201) and (116) planes. No other apparent peaks are observed, proving the absence of crystalline impurities.

According to the above observations, we summarize the growth processes and structural features of WS_2 NPs and WS_2 SCs. First, the structure of silica template is vital to the nanocasting process. In this study, the EP-FDU-12 silica template shows a unique mesostructure consisting of large mesopores and small wormlike mesopores. The structure of unique dual-mesoporous, which have a lot of highly interconnected pore channels, could enhance the mobility of precursors and create nanobridges between particles during nanocasting process. In addition, the morphologies and structures of the obtained products can be controlled by the filling amount of precursor, interior surface feature of silica template and reaction conditions. These factors are crucial to the growth process of the products within the silica mesoporous matrix.[29-31]

View Article Online
DOI: 10.1039/D0NR01130D

Among them, the filling amount of PTA precursor is the most important factor on the final structures of WS_2 products. With the increase of PTA concentration from 5 mM to 30 mM, the obtained morphologies of WS_2 nanostructures could be changed from multilayered WS_2 bowl, WS_2 half-sphere and WS_2 sphere to WS_2 SCs. According to the morphology characteristics of different WS_2 structures discussed in Figures 3 and 4, we infer the growth processes of WS_2 layers in the EP-FDU-12 silica template. For the synthesis of WS_2 bowls and half-spheres using PTA precursor with filling concentrations of 5 and 10 mM, the spherical cells in EP-FDU-12 template cannot be filled with PTA completely. After the high temperature reductive sulfuration process, the nanosized WS_2 layers grow crookedly along the spherical cell wall firstly. Then, the remaining WS_2 layers aggregate in the center of the spherical cells, resulting in the formation of WS_2 bowls and half-spheres. As the PTA concentration increase to 20 mM, initially, the spherical cells of EP-FDU-12 silica template are almost filled completely with PTA precursor, thus disordered and crooked WS_2 sheets can grow randomly and fill in the whole spherical cells to form WS_2 spheres after reductive sulfuration process. Further increasing the PTA concentration to 30 mM, not only the whole spherical cells are filled completely, but also the PTA precursor overflows along the mesopores on the cell walls, leading to the interconnection within the surrounding spherical cells. After the reductive sulfuration process at high temperature, the spherical cells are filled with nanosized WS_2 layers and the rest of nanosized WS_2 layers aggregate along the spherical cell channels and connect the adjacent spherical cell to form the WS_2 SCs structure. It should be noted that, in current growth processes of WS_2 nanostructures, the mass diffusion, migration and aggregation do not seem to be a dominated process, unlike the WO_3 growth system reported in our previous studies.[32]

Raman characteristics

Raman scattering has been widely applied to investigate the interior structure information of 2D materials. Since the estimated number of WS_2 layer is 8-12 in each WS_2 nanostructures, the

View Article Online
DOI: 10.1039/D0NR01130D

peaks in Raman spectra will be assigned following the rule of bulk TMDCs (Figures 5b and 5c).[33-40] Bulk WS_2 is 2*Hc* polytype with D_{6h}^4 ($P6_3/mmc$) symmetry. Its Raman active lattice vibrations at the Γ point of the hexagonal Brillion zone are A_{1g} (421 cm^{-1}), E_{2g}^1 (356 cm^{-1}), E_{2g}^2 (27 cm^{-1}) and E_{1g} (306 cm^{-1}), where the last mode is silent when the incident light with electric field is parallel to the basal plane.[41,42] Furthermore, second and higher order Raman transitions are observed for excitation energies close to the band gap, where the most prominent one is ascribed to the 2LA(M) band, originated from a second-order resonant process involving two longitudinal acoustic (LA) phonons close to the M point of the first Brillouin zone. Figure 5a schematically shows the typical vibration fashions of bilayer WS_2, such as A_{1g} and E_{2g}^1 modes, which contribute to the main features of Raman peaks in our experiment. In addition, B_{1u} mode is also schematically plotted, which is usually silent for planar 2D MX_2 structures. No photoluminescent emission can be observed in the synthesized WS_2 samples (Figure S2), which results from the multilayer feature of the structures.[43,44]

For multilayer WS_2, the direct band gap is at the K point and governed by a pair of excitons A and B (1.98 and 2.41 eV, respectively).[45] Therefore, the corresponding Raman intensities will be greatly enhanced and richer phonon vibration information can be observed when the wavelength of the excitation lasers is close to the excitonic energy. In our experiment, four lasers with wavelengths of 325, 532, 633 and 785 nm are employed to excite the Raman signals. Figure 5b shows the room-temperature Raman spectra of WS_2 NPs and SCs structures with the first- and second-order Raman features. A_{1g} (421 cm^{-1}) and E_{2g}^1 (356 cm^{-1}) can be obviously observed under the excitation of 325, 532 and 633 nm (Figure 5c). Interestingly, it is found that the Raman peak at ~ 421 cm^{-1} is enhanced and the second-order Raman features are more obvious under the excitation of 532 and 633 nm lasers, which are close to two excitonic energy. In contrast, no significant

View Article Online
DOI: 10.1039/D0NR01130D

Raman peak is observed for WS_2 NPs under the excitation of 785 nm laser since the excitation energy is much smaller than the optical transition energy.[37] Notably, since there is no significant difference in the Raman spectra of bowl-like, half-sphere-like and sphere-like WS_2 NPs (Figure S3), Raman signal from NPs will not be differentiated in the following study. By fitting the two prominent Raman peaks with Lorentizan functions, we obtain different vibration phonon modes in WS_2 NPs and SCs (Figure 5b).

As predicted by group theory, B_{1u} mode is Raman silent,[36] but it becomes Raman active in WS_2 nanotubes which arise from curved layers and structural disorder of WS_2.[35,37,39] Davydov splitting phenomenon has been extensively studied to explain the interlayer interaction in multilayer TMDCs.[46-49] B_{1u} mode is the Davydov couple of A_{1g} mode, which locates at the lower frequency side of A_{1g} mode (Figure 5a). To phenomenologically understand the B_{1u} mode: tungsten atoms stand still, while sulfur atoms vibrate out-of-phase (Figure 5a); as a result, the net vibration is zero due to the cancellation effect; when curvature or disorder are introduced, B_{1u} mode becomes active because of non-zero net vibration. The synthesized WS_2 NPs and SCs structures consist of curved, folded and interlaced WS_2 layers, as the HRETM images shown in Figures 3b, 3e, 3h and Figure 4d. Therefore, the silent B_{1u} mode at ~ 416 cm^{-1} becomes active in both WS_2 NPs and SCs structures under the excitation of 633 nm laser (Figure 5c). Nevertheless, the intensity of B_{1u} mode is still very weak since the curved features and disorder are not dominant.

Alternatively, exitonic resonances play a very important role in enhancing the intensity of B_{1u} mode. M. Staiger and colleagues showed that B_{1u} intensity can only be clearly observed at the excitation energy window ranging from 1.8 to 2.2 eV (A exciton, ~1.98 eV or ~626.3 nm in bulk WS_2), but it remains weak at the energy range of B exciton (~2.41 eV or ~514.5 nm in bulk WS_2),[37] which coincide with the results observed in this work. The differences between A and B excitons,

View Article Online
DOI: 10.1039/D0NR01130D

such as the effective mass and energy[50] will affect the interlayer interaction between WS_2 layers and thus result in an excitation-energy dependent Raman intensity enhancement.

To further study the properties of phonon in WS_2 NPs and SCs, Raman spectra are measured by varying the laser powers (Figures 6a, S4 and S5) and experimental temperatures (Figures 6b and S6) under the excitation of 532 and 633 nm lasers. Because of the different distribution characteristics, SC structures usually have lower power threshold in comparison with NP structures, which gives rise to the less data of SC structures. The frequencies of the hybrid modes at ~ 352 cm^{-1} for both types of WS_2 nanostructures have no significant difference as the laser power increases (Figures 6a and S7a). However, the relative intensity of 2LA mode at the lower energy shoulder of the Raman peak at ~ 352 cm^{-1} becomes stronger for larger excitation power for NP structures while such behavior is not obvious for SC structures. In particular, the B_{1u} mode turns active at ~ 420 cm^{-1} under the excitation of 633 nm. Figure 6b shows the Raman spectra measured by varying the temperature. The intensity ratio of 2LA and E^1_{2g} modes at ~ 352 cm^{-1} is insensitive to the temperature, whereas the case is complicated for modes at 420 cm^{-1}. Similar dependence of Raman peak redshift on the temperature increases has been observed for monolayer or few layers of WS_2 or other TMDCs.[14,15,51]

Overall, as the laser power increases, the Raman intensity ratio ($I_{(\sim420)}/I_{(\sim352)}$) increases only for WS_2 SCs under the excitation of 532 nm, while remains almost unchanged for other cases (Figure 7a). The Raman intensity ratio ($I_{(\sim420)}/I_{(\sim352)}$) decreases first and then increases as the temperature rises from 123 to 393 K (Figure 7b). Moreover, the frequency of the mode at ~ 420 cm^{-1} under the excitation of 532 nm redshifts slightly for both WS_2 nanostructures. The decrements $\Delta\omega$ are ~3.0 and ~3.8 cm^{-1} for WS_2 NPs and SCs, respectively (Figure S8), which match will the decrement $\Delta\omega$ reported in previous works at the same temperature range.[15,52-54]

View Article Online
DOI: 10.1039/D0NR01130D

The excitation of B_{1u} mode is one of the most important features of WS_2 containing curved layers. To further study the active B_{1u} and A_{1g} modes under the excitation of 633 nm laser, the Raman spectra are fitted by a set of Lorentzian functions. Figure 8 shows the dependence of peak position and Raman intensity radio ($I_{B_{1u}}/I_{A_{1g}}$)on the input laser powers and temperatures. As the laser power increases, the frequencies of the A_{1g} and B_{1u} modes redshift for WS_2 SCs whereas no significant change for WS_2 NPs. In our experiment, both WS_2 NPs and SCs are deposited on a silicon substrate. WS_2 NPs are loosely dispersed on Si substrate (Figure 2), while WS_2 SCs are tightly packed with a certain thickness (Figure 4). Under an irradiation of laser, only part of incident energy will interact with NPs, and the induced heat is easier to be conducted into the substrate. In a sharp contrast, all the incident energy will directly shine on the SCs. Therefore, the capability of heat conduction will be different for NP and SC samples. Higher local temperature is easier to be produced for WS_2 SC samples. Temperature change will affect both the exciton energy and the phonon energies, and thus the properties of Raman peaks, including intensity and peak position.[14,55] Consequently, Raman peaks of WS_2 SC samples are more sensitive to laser power. Moreover, the Raman peaks of WS_2 SCs are usually lower than the counterparts of NPs at room-temperature (Figure 8a, top panel), which is consistent with redshift in Raman peak caused by increases in temperature in previous works.[14,15,52-54] In comparison with the excitonic energy resonance, temperature change plays a minor role in affecting the Raman peaks. Under the excitation of 633 nm, Raman peaks decreases concurrently for both NP and SC samples (Figure 8b, top panel).

In comparison with A_{1g} mode, B_{1u} mode is barely present in flat 2D materials. However, its intensity $I_{B_{1u}}$ becomes comparable or even higher than $I_{A_{1g}}$ in the curved WS_2 nanostructures under the excitation of A exciton energy (Figure 8, lower panel). The intensity ratio ($I_{B_{1u}}/I_{A_{1g}}$) only varies slightly for both WS_2 nanostructures as laser power increases at room temperature (Figure 8a, lower

View Article Online
DOI: 10.1039/D0NR01130D

panel). Nevertheless, the intensity ratio decreases from 2 to 0.6 as the temperature increases from 123 to 393 K (Figure 8b, lower panel) for both WS_2 nanostructures. By checking the Raman spectra in Figure 6b, such a ratio reduction mainly ascribes to the decrease in the intensity of B_{1u} which indicates a lower B_{1u} mode excitation efficiency at higher temperature for the WS_2 nanostructures.

Roughly speaking, the above phenomena of Raman peak shift and intensity ratio variation can be attributed to the thermal effect induced by the input laser power and experimental temperature. Higher input power will increase the local temperature of samples and cause a Raman peak shift due to the resulted lattice changes.[55-57] In addition, the substrate may also play an important role in heat dissipation and then affect the lattice vibration.[14] In our experiment, both WS_2 SCs and WS_2 NPs are dispersed on a silicon substrate. The induced heat is easier to be transferred into the substrate from well-dispersed WS_2 NPs, in comparison with tightly packed WS_2 SCs. Therefore, the Raman features of WS_2 SCs are relatively easier to be affected by the excitation power, which are also verified by the larger power-dependent variations in peak position and intensity range. Nevertheless, the dependence of Raman properties on the laser power and temperature is more complex due to the complexity of synthesized structures themselves. As indicated by the TEM shown in Figures 2-4, the number, orientation and curvature of WS_2 layers varies spatially in the structures.

3. Conclusions

To conclude, WS_2 NPs and highly ordered WS_2 SCs with uniform and controllable geometric structure are synthesized by nanocasting processes using ordered mesoporous silica as the template. Due to the curved and interlaced multiple layers, their Raman signal is distinctly different from the counterparts of layered WS_2. Significantly, the curved features of WS_2 make the silent phonon mode active, which indicate a complex interior lattice vibration manner in comparison with planar structures. The main features of Raman peaks show different dependence on the excitation lasers,

View Article Online
DOI: 10.1039/D0NR01130D

including power and wavelength, and temperature, which thus provides a promising approach to manipulate the optical response of WS_2 structures. Therefore, we believe that 2D materials with curved morphology have greatly potential to provide novel optoelectronic properties for practical applications.

4. Experiment Section

Materials

Phosphotungstic acid (PTA, $H_3PW_{12}O_{40}•nH_2O$, 99.9%) is purchased from Sigma Aldrich. Anhydrous ethanol (C_2H_5OH, 99.7%), hydrofluoric acid (HF, 40%), sodium hydroxide (NaOH, 99.9%) are purchased from Sinopharm Chemical Industry Co., Ltd. All chemicals are directly used without any further purification.

Synthesis

Mesoporous silica template, EP-FDU-12, is synthesized following the approach reported in previous paper.[58] As a typical procedure, 10 mg of EP-FDU-12 silica template are immersed and dispersed into the ethanol solution of PTA (20 mM, 1 ml) under stirring for 10 min. The mixture was dried at 40 °C until ethanol is fully evaporated. After the complete drying, the obtained white powders of PTA/EP-FDU-12 silica template composites are put into a tube furnace for reductive sulfuration. The furnace is heated to 600 °C at a rate of 2 ºC/min under 5% H_2S/95% N_2 atmosphere and maintained at this temperature for 2 hrs. The tube furnace is connected a collector with sodium hydroxide solution to react with excess H_2S gas. After cooling down the furnace to room temperature, the dark brown WS_2/EP-FDU-12 powders are collected and treated by 5 mL of 4 wt % HF aqueous solution to etch silica. Finally, WS_2 products are collected by washing with water and acetone. In experiment, the concentration of the ethanol solution of PTA increases from 5 to 30 mM.

Characterizations

View Article Online
DOI: 10.1039/D0NR01130D

The morphology and structure of samples are characterized by scanning electron microscope (SEM, JEOL, JSM-7000F) and transmission electron microscope (TEM, JEOL, JEM-2100F with an accelerating voltage of 200 kV). The chemical composition of the product is characterized using X-ray diffraction (XRD, Bruker, d8 advance). Raman spectra are collected using JY Horiba HR800 Raman system under the excitation of 325, 532, 633 and 785 nm lasers. The laser beam is focused on the sample surface with a spot diameter of ~1 μm using a 50× long-working-distance lens (NA = 0.5) and the laser power is measured at the focal plane. The power-dependent Raman measurements are carried out at room temperature.

The temperature-dependent measurements are carried out with a 50× long-working-distance lens. A Linkam TS1500 heating system is used to heat the samples at increments of 30 °C and a heating rate of 10 °C/min. Before acquiring the spectrum, the temperature is held for at least five minutes at each temperature, allowing enough time for stabilization.

Conflict of Interest

The authors declare no conflict of interest

Acknowledgements

This work was supported by the National Natural Science Foundation of China (No. 21675122, 21874104), the State's Key Project of Research and Development Plan (2017YFB0402800), the World-Class Universities (Disciplines) and the Characteristic Development Guidance Funds for the Central Universities.

References

1 X. Duan, C. Wang, A. Pan, R. Yu and X. Duan, *Chem. Soc. Rev.*, 2015, **44**, 8859-8876.

2 K. F. Mak and J. Shan, *Nat. Photon.*, 2016, **10**, 216-226.

View Article Online
DOI: 10.1039/D0NR01130D

3 S. Manzeli, D. Ovchinnikov, D. Pasquier, O. V. Yazyev and A. Kis, *Nat. Rev. Mater.*, 2017, **2**, 170033.

4 X. Xu, W. Yao, D. Xiao and T. F. Heinz, *Nat. Phys.*, 2014, **10**, 343-350.

5 F. Xia, H. Wang, D. Xiao, M. Dubey and A. Ramasubramaniam, *Nat. Photon.*, 2014, **8**, 899-907.

6 W. Zhao, Z. Ghorannevis, L. Chu, M. Toh, C. Kloc, P.-H. Tan and G. Eda, *ACS Nano*, 2013, **7**, 791-797.

7 D. Voiry, H. Yamaguchi, J. Li, R. Silva, D. C. B. Alves, T. Fujita, M. Chen, T. Asefa, V. B. Shenoy, G. Eda and M. Chhowalla, *Nat. Mater.*, 2013, **12**, 850-855.

8 J. Song, L. Zhang, Y. Xue, Q. Y. S. Wu, F. Xia, C. Zhang, Y.-L. Zhong, Y. Zhang, J. Teng, M. Premaratne, C.-W. Qiu and Q. Bao, *ACS Photon.*, 2016, **3**, 1986-1992.

9 X. Chen, W. Fan and C. Song, *Carbon*, 2018, **133**, 416-422.

10 L. Yadgarov, C. L. Choi, A. Sedova, A. Cohen, R. Rosentsveig, O. Bar-Elli, D. Oron, H. Dai and R. Tenne, *ACS Nano*, 2014, **8**, 3575-3583.

11 A. Yella, M. Panthoefer, M. Kappl and W. Tremel, *Angew. Chem. Int. Edit.*, 2010, **49**, 2575-2580.

12 B. R. Carvalho, L. M. Malard, J. M. Alves, C. Fantini and M. A. Pimenta, *Phys. Rev. Lett.*, 2015, **114**.

13 Y. Zhao, X. Luo, H. Li, J. Zhang, P. T. Araujo, C. K. Gan, J. Wu, H. Zhang, S. Y. Quek, M. S. Dresselhaus and Q. Xiong, *Nano Lett.*, 2013, **13**, 1007-1015.

14 R. Yan, J. R. Simpson, S. Bertolazzi, J. Brivio, M. Watson, X. Wu, A. Kis, T. Luo, A. R. H. Walker and H. G. Xing, *ACS Nano*, 2014, **8**, 986-993.

15 A. P. S. Gaur, S. Sahoo, J. F. Scott and R. S. Katiyar, *J. Phys. Chem. C*, 2015, **119**, 5146-5151.

16 Y. Wang, C. Cong, C. Qiu and T. Yu, *Small*, 2013, **9**, 2857-2861.

17 Y. Zhang, Y. Zhang, Q. Ji, J. Ju, H. Yuan, J. Shi, T. Gao, D. Ma, M. Liu, Y. Chen, X. Song, H.

View Article Online
DOI: 10.1039/D0NR01130D

Y. Hwang, Y. Cui and Z. Liu, *ACS Nano*, 2013, **7**, 8963-8971.

18 H.-C. Kim, H. Kim, J.-U. Lee, H.-B. Lee, D.-H. Choi, J.-H. Lee, W. H. Lee, S. H. Jhang, B. H. Park, H. Cheong, S.-W. Lee and H.-J. Chung, *ACS Nano*, 2015, **9**, 6854-6860.

19 K. Wang, B. Huang, M. Tian, F. Ceballos, M.-W. Lin, M. Mahjouri-Samani, A. Boulesbaa, A. A. Puretzky, C. M. Rouleau, M. Yoon, H. Zhao, K. Xiao, G. Duscher and D. B. Geohegan, *ACS Nano*, 2016, **10**, 6612-6622.

20 L. P. McDonnell, C.-C. Huang, Q. Cui, D. W. Hewak and D. C. Smith, *Nano Lett.*, 2018, **18**, 1428-1434.

21 R. Tenne, L. Margulis, M. Genut and G. Hodes, *Nature*, 1992, **360**, 444-446.

22 Y. Feldman, E. Wasserman, D. J. Srolovitz and R. Tenne, *Science*, 1995, **267**, 222-225.

23 I. Alexandrou, N. Sano, A. Burrows, R. R. Meyer, H. Wang, A. I. Kirkland, C. J. Kiely and G. A. J. Amaratunga, *Nanotechnology*, 2003, **14**, 913-917.

24 C. Schuffenhauer, R. Popovitz-Biro and R. Tenne, *J. Mater. Chem.*, 2002, **12**, 1587-1591.

25 P. A. Parilla, A. C. Dillon, B. A. Parkinson, K. M. Jones, J. Alleman, G. Riker, D. S. Ginley and M. J. Heben, *J. Phys. Chem. B*, 2004, **108**, 6197-6207.

26 D. Vollath and D. V. Szabo, *Acta Mater.*, 2000, **48**, 953-967.

27 M. Remskar, A. Mrzel, Z. Skraba, A. Jesih, M. Ceh, J. Demsar, P. Stadelmann, F. Levy and D. Mihailovic, *Science*, 2001, **292**, 479-481.

28 S. Bastide, D. Duphil, J. P. Borra and C. Levy-Clement, *Adv. Mater.*, 2006, **18**, 106-109.

29 Y. Shi, Y. Wan, R. Liu, B. Tu and D. Zhao, *J. Am. Chem. Soc.*, 2007, **129**, 9522-9531.

30 C. Tian, Y. Deng, D. Zhao and J. Fang, *Adv. Opt. Mater.*, 2015, **3**, 404-411.

31 J. Fang, L. Zhang, J. Li, L. Lu, C. Ma, S. Cheng, Z. Li, Q. Xiong and H. You, *Nat. Commun.*, 2018, **9**, 251.

32 L. Zhang, J. Li, H. You, C. Ma, S. Lan, Z. Wu, J. Zeng, F. Tian and J. Fang, *Small*, 2018, **14**,

View Article Online
DOI: 10.1039/D0NR01130D

1702565.

33. J. L. Verble and T. J. Wieting, *Phys. Rev. Lett.*, 1970, **25**, 362-365.
34. X. Zhang, X.-F. Qiao, W. Shi, J.-B. Wu, D.-S. Jiang and P.-H. Tan, *Chem. Soc. Rev.*, 2015, **44**, 2757-2785.
35. M. Krause, M. Virsek, M. Remskar, N. Salacan, N. Fleischer, L. Chen, P. Hatto, A. Kolitsch and W. Moeller, *Chemphyschem*, 2009, **10**, 2221-2225.
36. A. Molina-Sanchez and L. Wirtz, *Phys. Rev. B*, 2011, **84,** 155413.
37. M. Staiger, P. Rafailov, K. Gartsman, H. Telg, M. Krause, G. Radovsky, A. Zak and C. Thomsen, *Phys. Rev. B*, 2012, **86,** 165423.
38. N. Scheuschner, R. Gillen, M. Staiger and J. Maultzsch, *Phys. Rev. B*, 2015, **91,** 235409.
39. K. R. O'Neal, J. G. Cherian, A. Zak, R. Tenne, Z. Liu and J. L. Musfeldt, *Nano Lett.*, 2016, **16**, 993-999.
40. A. Berkdemir, H. R. Gutierrez, A. R. Botello-Mendez, N. Perea-Lopez, A. L. Elias, C.-I. Chia, B. Wang, V. H. Crespi, F. Lopez-Urias, J.-C. Charlier, H. Terrones and M. Terrones, *Sci. Rep.*, 2013, **3,** 1755.
41. T. Sekine, T. Nakashizu, K. Toyoda, K. Uchinokura and E. Matsuura, *Solid State Commun.*, 1980, **35**, 371-373.
42. C. Sourisseau, F. Cruege, M. Fouassier and M. Alba, *Chem. Phys.*, 1991, **150**, 281-293.
43. A. Splendiani, L. Sun, Y. Zhang, T. Li, J. Kim, C.-Y. Chim, G. Galli and F. Wang, *Nano Lett.*, 2010, **10**, 1271-1275.
44. K. F. Mak, C. Lee, J. Hone, J. Shan and T. F. Heinz, *Phys. Rev. Lett.*, 2010, **105,** 136805.
45. C. Ballif, M. Regula and F. Levy, *Sol. Energ. Mater. Sol. C.*, 1999, **57**, 189-207.
46. Q.-H. Tan, Y.-J. Sun, X.-L. Liu, Y. Zhao, Q. Xiong, P.-H. Tan and J. Zhang, *2D Mater.*, 2017, **4,** 031007.

View Article Online
DOI: 10.1039/D0NR01130D

47. Q. J. Song, Q. H. Tan, X. Zhang, J. B. Wu, B. W. Sheng, Y. Wan, X. Q. Wang, L. Dai and P. H. Tan, *Phys. Rev. B*, 2016, **93,** 115409.

48. P. Tonndorf, R. Schmidt, P. Boettger, X. Zhang, J. Boerner, A. Liebig, M. Albrecht, C. Kloc, O. Gordan, D. R. T. Zahn, S. M. de Vasconcellos and R. Bratschitsch, *Opt. Express*, 2013, **21**, 4908-4916.

49. K. Kim, J.-U. Lee, D. Nam and H. Cheong, *ACS Nano*, 2016, **10**, 8113-8120.

50. R. Coehoorn, C. Haas and R. A. Degroot, *Phys. Rev. B*, 1987, **35**, 6203-6206.

51. S. Sahoo, A. P. S. Gaur, M. Ahmadi, M. J. F. Guinel and R. S. Katiyar, *J. Phys. Chem. C*, 2013, **117**, 9042-9047.

52. L. Su, Y. Yu, L. Cao and Y. Zhang, *Nano Res.*, 2015, **8**, 2686-2697.

53. X. Huang, Y. Gao, T. Yang, W. Ren, H.-M. Cheng and T. Lai, *Sci. Rep.*, 2016, **6,** 32236.

54. M. Thripuranthaka and D. J. Late, *ACS Appl. Mater. Inter.*, 2014, **6**, 1158-1163.

55. T. Beechem, S. Graham, S. P. Kearney, L. M. Phinney and J. R. Serrano, *Rev. Sci. Instrum.*, 2007, **78,** 061301.

56. R. A. Cowley, *Adv. Phys.*, 1963, **12**, 421-480.

57. M. S. Liu, L. A. Bursill, S. Prawer and R. Beserman, *Phys. Rev. B*, 2000, **61**, 3391-3395.

58. G. Ma, X. Yan, Y. Li, L. Xiao, Z. Huang, Y. Lu and J. Fan, *J. Am. Chem. Soc.*, 2010, **132**, 9596-9597.

View Article Online
DOI: 10.1039/D0NR01130D

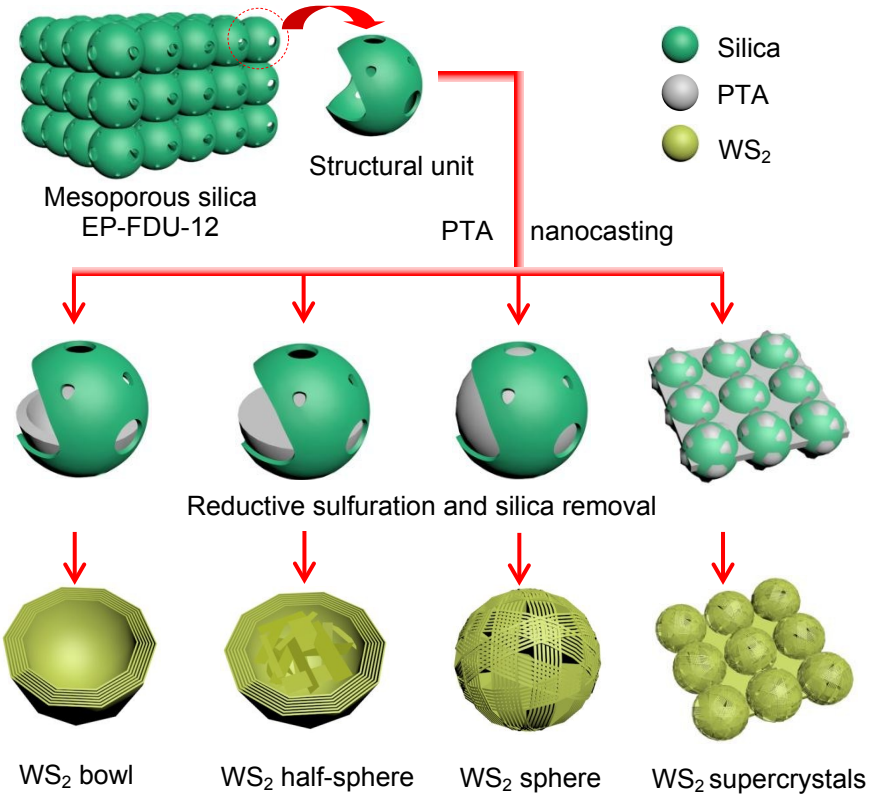

Figure 1. The schematic of the fabrication process of WS_2 NPs and SCs *via* nanocasting method using EP-FDU-12 mesoporous silica as the hard template.

View Article Online
DOI: 10.1039/D0NR01130D

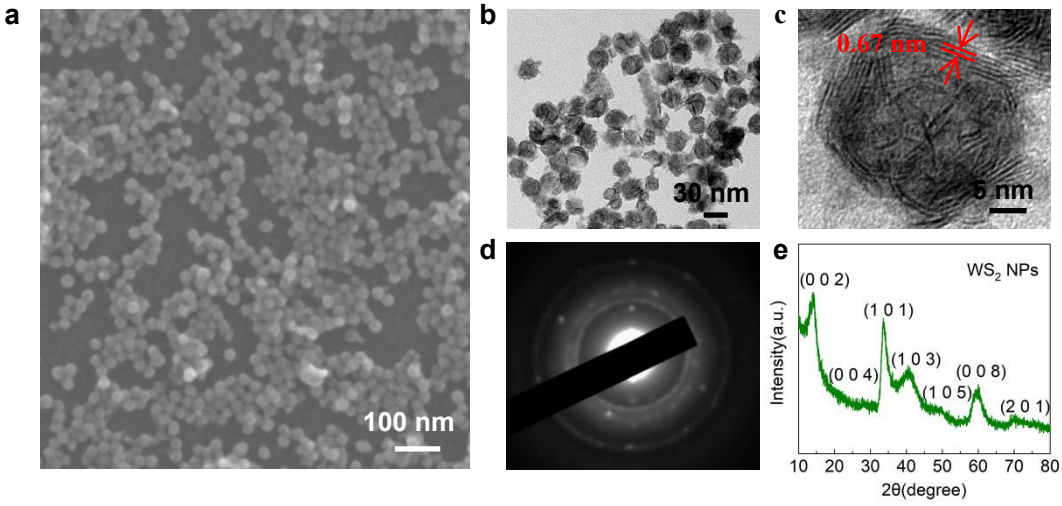

Figure 2. The typical structural characterizations of WS_2 NPs. The typical (a) SEM and (b) low-magnification TEM images of WS_2 NPs. (c) HRTEM images of one isolated WS_2 NP. (d) The corresponding SAED pattern of (b). (e) XRD pattern of the WS_2 NPs.

View Article Online
DOI: 10.1039/D0NR01130D

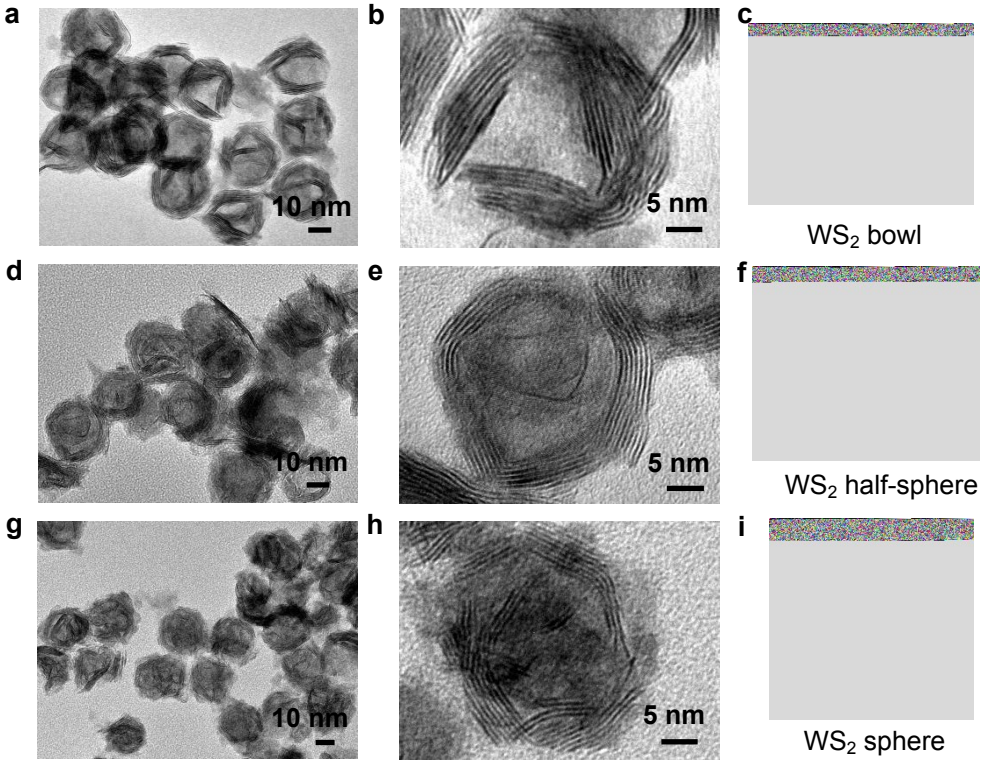

Figure 3. TEM images and the schematics of three different morphologies produced by changing the filling amounts of PTA. (a)-(c) are the low-magnification, high magnification TEM image, and schematic of the WS_2 bowl. (d)-(f) and (g)-(i) are the counterparts of the WS_2 half-sphere and WS_2 sphere, respectively. The filling amounts of PTA for the three types of NPs are (5 mM, 1 ml), (10 mM, 1 ml), and (20 mM, 1 ml), respectively, from the top to the bottom.

View Article Online
DOI: 10.1039/D0NR01130D

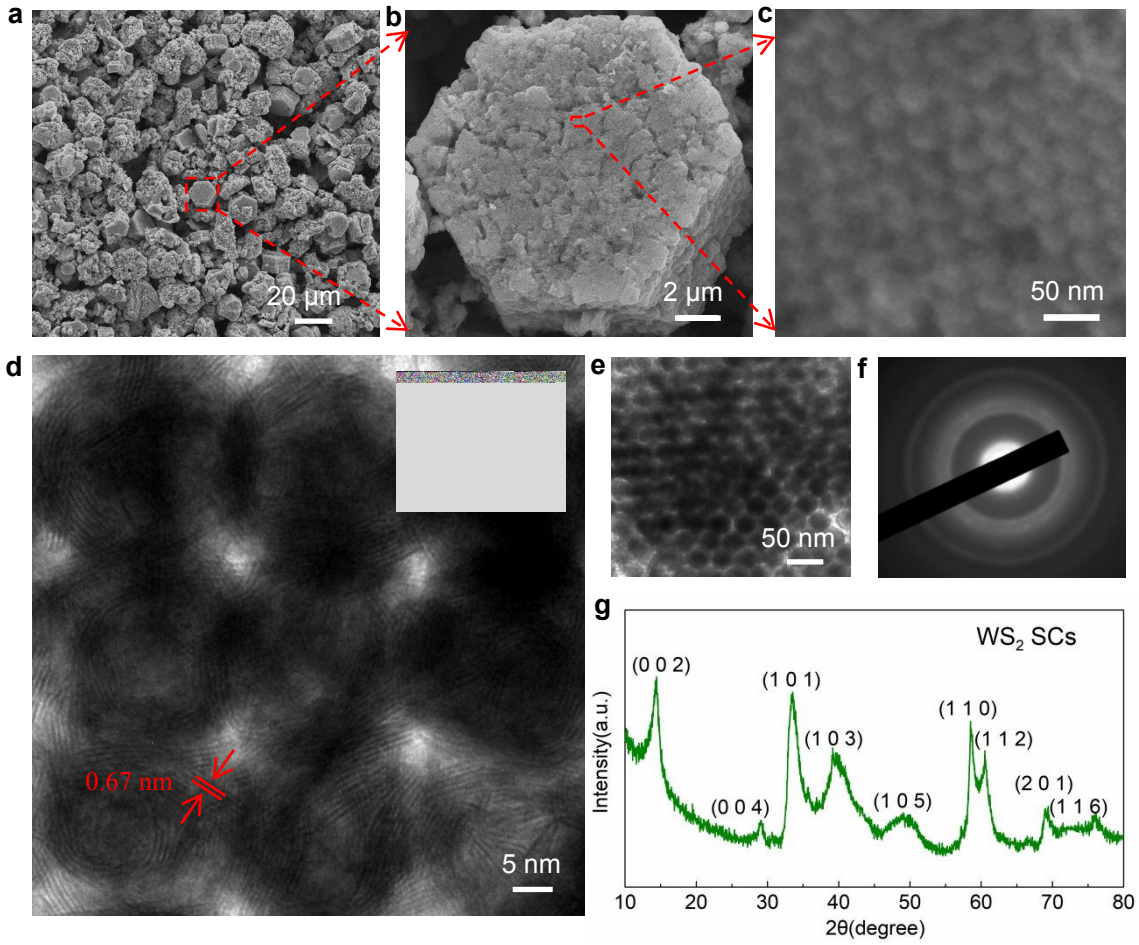

Figure 4. The structural characterizations of WS_2 SCs. (a)-(c) The low-magnified, high-magnified and enlarged images of WS_2 SCs. (d)-(e) HRTEM images of WS_2 SCs. (f) The corresponding SAED pattern of (d). (g) XRD pattern of the WS_2 SCs.

View Article Online
DOI: 10.1039/D0NR01130D

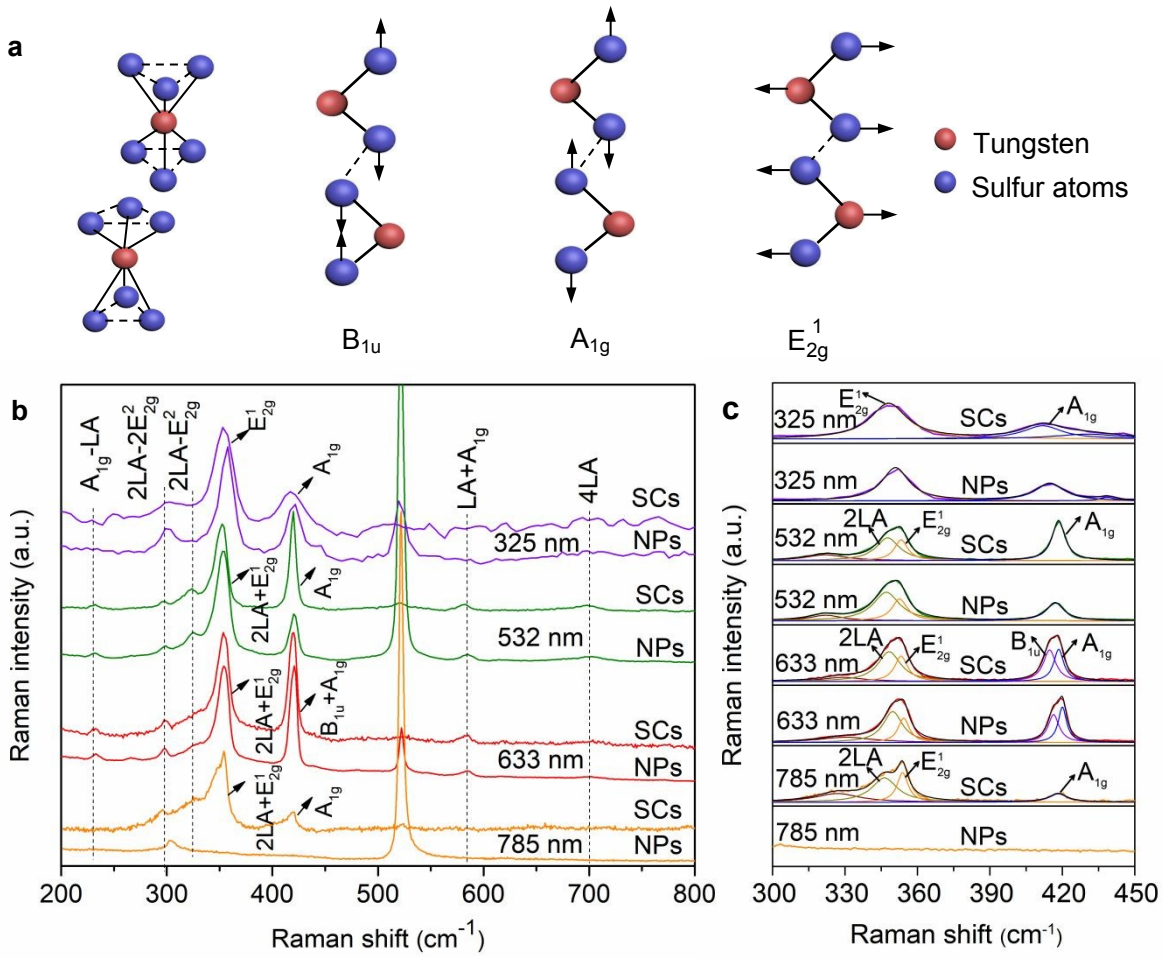

Figure 5. Typical phonon vibration modes of WS_2 and Raman spectra of WS_2 NPs and WS_2 SCs. (a) The schematics of the phonon vibration modes in a bilayer WS_2 system. (b) Raman spectra of WS_2 NPs and WS_2 SCs. (c) Detailed Raman spectra of WS_2 NPs and SCs with significant features at the zoom-in frequency range. The Raman spectra are measured under the excitation of 325, 532, 633, and 785 nm lasers.

View Article Online
DOI: 10.1039/D0NR01130D

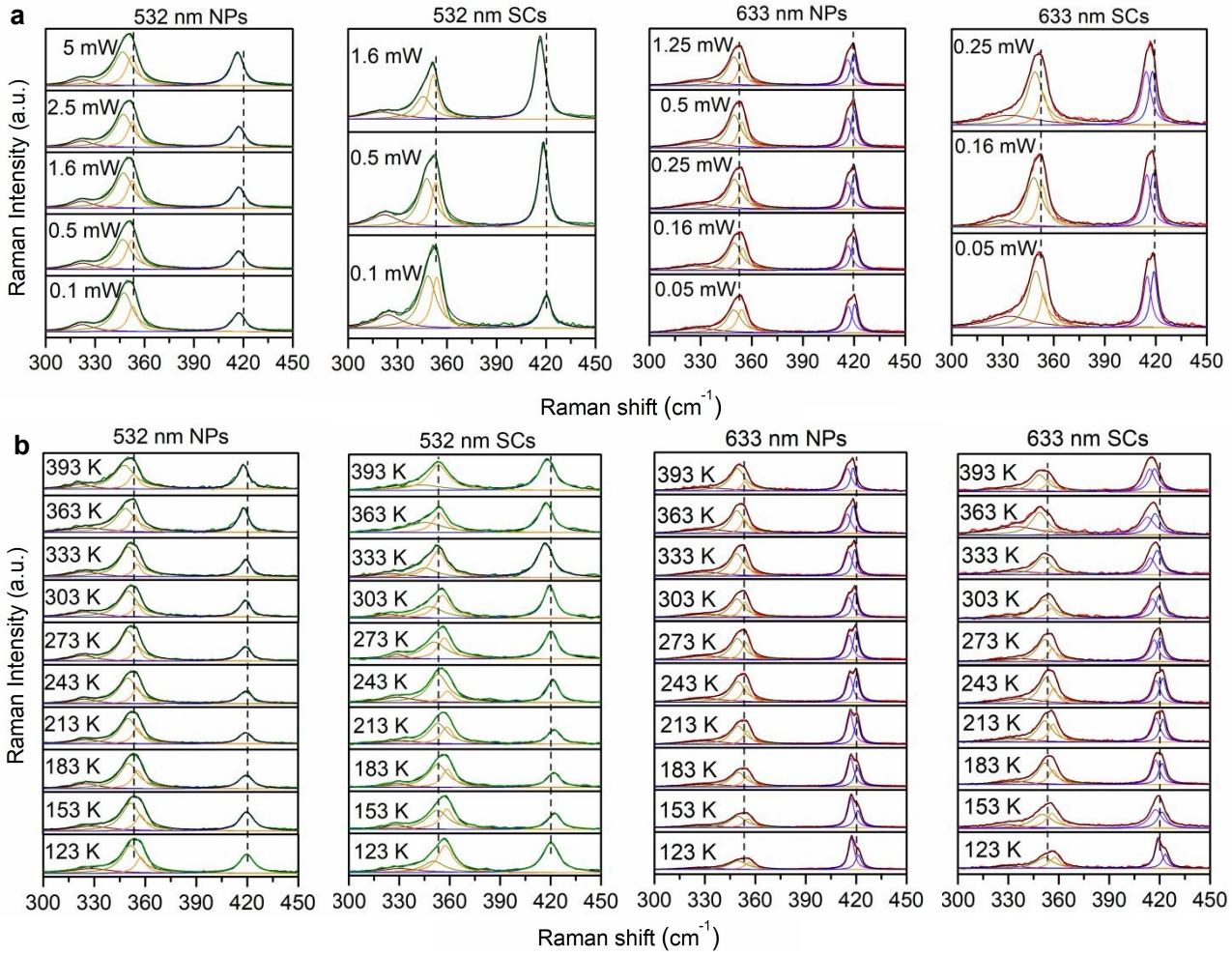

Figure 6. Dependence of Raman spectra of WS_2 NPs and SCs on the excitation (a) laser powers and (b) temperature. The laser powers are 0.5 mW for 532 nm laser and 0.16 mW for 633 nm laser when measuring the temperature-dependent Raman spectra. Colorful lines are the fitted curves with a set of Lorentzian functions.

View Article Online
DOI: 10.1039/D0NR01130D

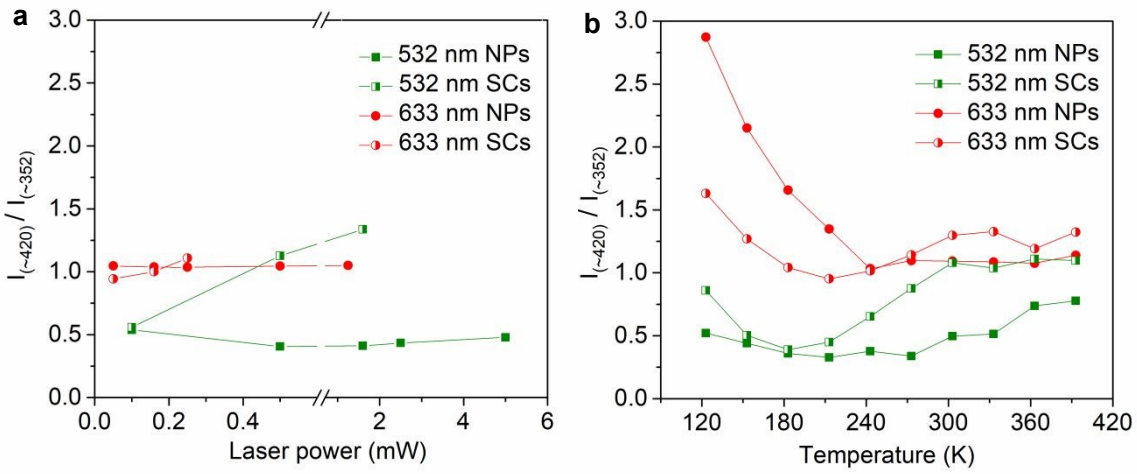

Figure 7. Dependence of Raman intensity ratio of the two prominent Raman peaks ~420 and ~352 cm^{-1} on the (a) laser power and (b) temperature. All the Raman peaks are obtained under the excitation of 532 and 633 nm lasers.

View Article Online
DOI: 10.1039/D0NR01130D

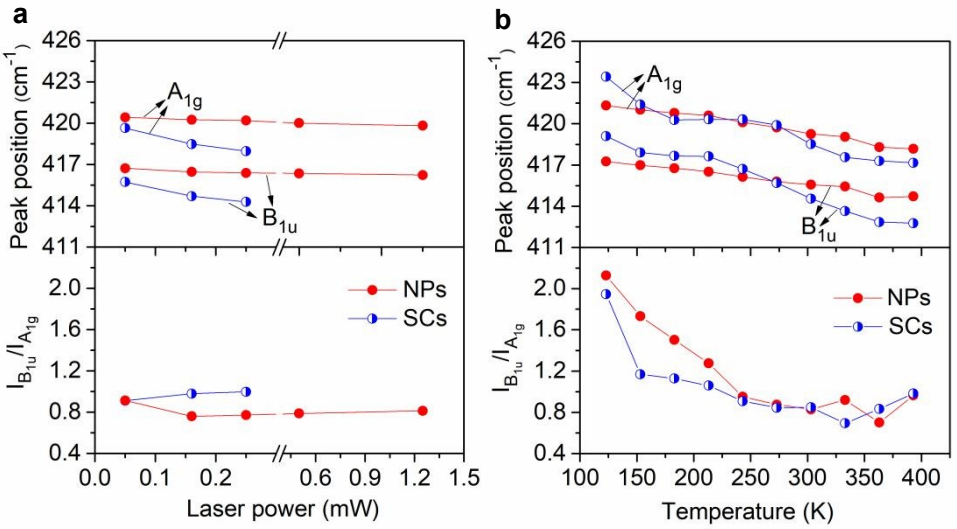

Figure 8. Dependence of Raman peak position and intensity radio of A_{1g} and B_{1u} modes on (a) laser power at room temperature and (b) temperature. Raman signal are excited by 633 nm lasers.